Improving wavefront sensing with a Shack–Hartmann device

Martin Rais,[1,2,*] Jean-Michel Morel,[2] Carole Thiebaut,[3] Jean-Marc Delvit,[3] and Gabriele Facciolo[2,4]

[1]TAMI, Universitat des les Illes Balears, Carretera de Valdemosa km 7.5, Mallorca, Spain
[2]CMLA, ENS Cachan, Université Paris Saclay, 63 Avenue du President Wilson, 94235 Cachan CEDEX, France
[3]CNES, 18 Avenue Edouard Belin, 31400 Toulouse, France
[4]LIGM (UMR CNRS 8049), ENPC, Université Paris-Est, France
*Corresponding author: martin.rais@cmla.ens-cachan.fr

To achieve higher resolutions, current earth observation satellites use larger, lightweight primary mirrors that can deform over time, affecting the image quality. To overcome this problem, we evaluated the possibility of combining a deformable mirror with a Shack–Hartman wavefront sensor (SHWFS) directly in the satellite. The SHWFS's performance depends entirely on the accuracy of the shift estimation algorithm employed, which should be computationally cheap to execute onboard. We analyzed the problem of fast, accurate shift estimation in this context and have proposed a new algorithm, based on a global optical flow method that estimates the shifts in linear time. Based on our experiments, we believe our method has proven to be more accurate and stable, as well as less sensitive to noise, than all current state-of-the-art methods, permitting a more precise onboard wavefront estimation. © 2016 Optical Society of America

1. INTRODUCTION

Adaptive optics (AO) is a well-known technology to sense and correct wavefront distortions. This technology is used in astronomy to produce sharper images from heavily aberrated wavefronts caused by atmospheric turbulence. This correction is usually performed through a deformable mirror that adapts to the measured wavefront and corrects the distortion [1]. Since AO also helps to improve the performance of aberrated optical systems, it is widely used in several other contexts, including ophthalmology [2], microscopy [3], and free-space laser communication systems [4], among others [5].

A key component of an AO system is its wavefront sensing mechanism (i.e., the device used to precisely measure distortion). A Shack–Hartmann wavefront sensor (SHWFS) is one such device. It uses an array of lenslets to measure the deformation of an incoming wavefront. The shift of each lenslet focal plane image is proportional to the mean slope of the wavefront in the subaperture onto this lenslet. It yields a discrete local approximation of the wavefront's slope (Fig. 1). This deformation is usually measured by imaging a point source such as a star, and measuring the relative displacement between a reference image and all other subimages to compute the wavefront's local gradient.

Recently, the community evaluated correcting wavefront deformations on earth observation satellites [6–8] caused by the deformation of the primary mirror. In this setting, the problem of atmospheric turbulence is negligible. Indeed, in astronomical observations from the earth, the angle of view is extremely narrow. As a result, the light wavefront crosses a narrow solid angle of atmosphere and its perturbations due to turbulence have a great affect on image quality. In earth observation from a satellite, however, the viewing angle is much larger, so perturbations due to turbulence are relatively much smaller.

The correction of optical aberration, however, is becoming more and more important for high-resolution earth observation satellites. To increase the spatial resolution of satellite images (i.e., the ground sample distance), a larger primary mirror is required to gain a higher angular resolution. Large mirrors must be thicker to avoid deformations, which dramatically increases their weight and makes launching costs prohibitive. For this reason, large, but lighter, mirrors must be considered. One drawback of lighter mirrors, though, is that time-varying deformations due to thermal effects and vibration severely deteriorate the image quality [9]. To correct these deformations, a SHWFS device could be used to measure them by observing
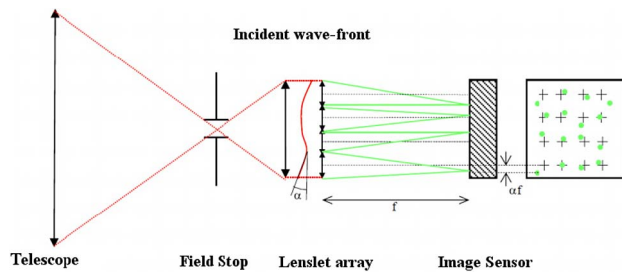
Fig. 1. Shack–Hartmann wave-front sensor measures the wave-front by computing the local shifts between the detected spots (in green) and the reference crosses (in black), which would occur if no deformation were present.

(a) Occlusion schema in a 12 × 12 SHWFS.

(b) Images obtained on an extended landscape.

Fig. 2. Example of a SHWFS occlusion scheme under a Korsch telescope. Both the secondary mirror and the arms used to hold it are clearly visible. For each lenslet, the decrease of the incoming signal is proportional to its occlusion.

the earth together with a deformable mirror to compensate for these deformations. As opposed to AO, where the distortion must be compensated in real-time due to the fast changes in the atmosphere, the compensation needed for the mirror deformation is less frequent, roughly just seconds.

Coming from the control theory, two schemes exist to perform wavefront correction. In an *open loop* system, the wavefront error is measured before the wavefront corrector corrects it. In a *closed loop* system, however, the measured wavefront deformation is the residual error after the correction of the previous estimation. The difference between both operational modes is important because in a *closed loop* system, the wavefront aberrations measured will be small, which allows to assume a maximum shift between images of up to a few pixels. In this paper we assumed a *closed loop* system.

Another important factor that affects the accuracy of wavefront sensing is the phenomenon of scintillation and phase anisoplanatism, which results in more complex patterns than simple global shifts between subapertures. The influence of this phenomenon was widely studied in the context of AO [10–12]. However, in remote sensing, because the phase aberration is produced at the telescope pupil, all parts of the image are affected by it in the same way, neglecting its incidence [10].

Finally, once the shift estimation is performed, several methods can be used to reconstruct the wavefront from its local gradient estimations, namely the iterative zonal method [13], the vector-matrix-multiply (VMM) method [14], and the Fourier transform reconstruction (FTR) method [15]. The latter is recommended when the number of actuators is high. The VMM method, however, obtains more accurate results under a SHWFS configuration using less than 12 × 12 subapertures [16].

As mentioned before, wavefront sensing in astronomy is usually performed using the stars. When observing the earth from space this task becomes more challenging.

Extended scene versus point source observation. For an earth observation satellite, the SHWFS is used on extended scenes instead of point sources such as stars. This setup is called scene-based wavefront sensing (SBWFS), or extended-scene wavefront sensing (ESWFS). Because the scene is extended, a field stop must be installed in front of the SHWFS, as seen in Fig. 1, so the images given by the lenslet array do not overlap in the lenslet focal plane [17]. This yields a grid of images, each
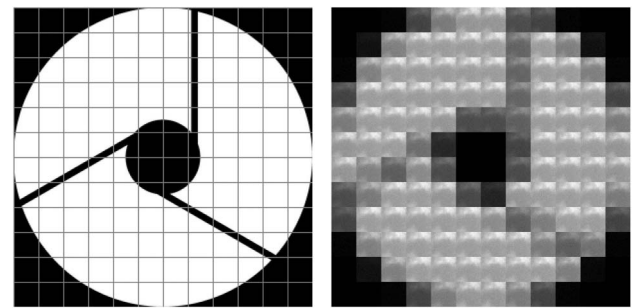
one corresponding to one subaperture, which are shifted versions of the same scene. By accurately measuring these shifts, we can estimate the wavefront's gradient. Since we are dealing with landscapes larger than the captured image, however, it becomes challenging to accurately perform the shift estimation. Even worse, in most wavefront sensors, the extent of the source object normally reduces the contrast of the signal, further thwarting accurate shift measurements [18].

Difference in subimage SNRs due to pupil occlusions. For long focal length telescopes commonly used on earth observation satellites, the Korsch concept is the most common. The pupil of a Korsch telescope is generally occluded in the center by a secondary mirror. The arms used to hold this mirror also occlude the pupil. In these regions, the lenslets suffer a loss in the incoming signal, proportional to the percentage of occlusion. Figure 2(a) depicts this configuration. Figure 2(b) shows an example of a SHWFS output in the CRT sensor, which shows how the signal-to-noise ration (SNR) on the partially occluded lenslets is significantly lower.

Limited onboard computational capacity. An important distinction when performing wavefront sensing from earth observation satellites is its limited computational capacity. Because of this constraint, several shift estimation methods proposed for SHWFS are not suitable onboard due to their high complexity.

Unusable observations. Another difference when observing extended scenes, as opposed to the use of SHWFS with point sources, is the need to predict if the current scene allows to accurately estimate the wavefront aberration. Scenes such as clouds, the sea, or any textureless landscape can thwart all shift measurement methods, leading to poor wavefront estimation.

Contributions. Based on these differences, here we have presented a new shift estimation method in the context of SHWFS used on extended scenes. Our contribution is three-fold. First, we reviewed state-of-the-art on wavefront correction using SHWFS on extended scenes. Second, we have proposed the use of an iterative global optical flow method for shift estimation that presents several advantages over conventional correlation methods. Third, we have proposed a fast and effective method for scene pre-selection that adds almost no further computational cost to the overall estimation using the proposed algorithm.

Section 2 reviews the state-of-the-art on shift estimation applied for SHWFS on extended scenes. Section 3 presents our optical flow method and its usage for wavefront correction from earth observation satellites. Section 4 focuses on scene preselection methods. Section 5 examines the influence of the parameters on the proposed method, and thoroughly compares its performance with state-of-the-art options. Here, we used ground truth simulations provided by CNES and our own simulator. Finally, Section 6 offers our conclusions.

2. STATE-OF-THE-ART REVIEW

Since the Shack–Hartmann wavefront sensor was introduced in the late 1960s [19], several algorithms have been proposed to estimate the shifts using point sources such as stars. However, only few authors have studied the problem when the source is extended, as when observing the earth from space. Broadly, they can be categorized in correlation methods working in the spatial [17,20,21] or in the frequency domain [6,21–24]; phase correlation methods that estimate the shift directly in the frequency domain [24,25]; iterative methods [22,23] that improve on previous approaches by progressively estimating the shift; and maximum likelihood (ML) approaches [26] that incorporate a specific noise model and compute the ML estimate as the solution to an optimization problem.

A. Correlation-based Methods

These methods compute a correlation score on a grid $C(i, j)$ and interpolate it to determine the subpixel location of the peak. The methods mainly differ in the choices of correlation score and interpolation strategy.

Spatial domain correlation-based methods. Michau *et al.* [20] were among the first to propose an experimental implementation that used a SHWFS on extended sources larger than the wavefront sensor field of view. Their method computes the discrete cross-correlation between the images and a reference subimage chosen from the central region of the wavefront sensor image pattern. To estimate the subpixel shifts, the correlation peak location is computed as the centroid of the pixels with a correlation higher than half the maximal observed correlation.

Löfdahl [21] tested several shift estimation algorithms for Shack–Hartmann wavefront sensors observing the sun. By testing using several possible sources of errors such as noise, blur, and bias mismatch, he evaluated five different correlation-based methods to obtain the correlation score $C(i, j)$. Among the evaluated correlation algorithms, the best all-around performer proved to be the classical least squares approach or squared difference function (SDF). Another proposed correlation score is the covariance function in the image domain (CFI) using trend-corrected versions of both images. Indeed, Smithson and Tarbell [27] showed that a linear trend in intensity shifts the covariance peak from the correct position, so a fitted plane must be subtracted from both images beforehand. For the SHWFS case, this task amounts to simply subtracting the mean value for each image. They also tested other two methods based on the absolute difference between both images (ADF), and its square (ADF²) to better locate the minimum at the subpixel level.

To achieve subpixel precision, they evaluated four interpolation strategies to look for the minimum value on the correlation grid $C(i_{\min}, j_{\min})$. The four algorithms they evaluated can be described as fitting a conic section to the 3 × 3-element submatrix s centered in the sample minimum $C(i_{\min}, j_{\min})$. The evaluated algorithms differ on the number of pixels used and on whether the fitting is done in a two-dimensional (2D) environment or in each dimension separately. The 1D quadratic interpolation (1QI) fits a parabola in each dimension independently, while the 2D quadratic interpolation (2QI) fits the conic to the 3 × 3 neighborhood. They also evaluated a 1D least square (1LS) method on both dimensions, which averages the three values on one dimension and then applies least squares on the other, and a 2D least square (2LS) variant, which includes the corner values in the procedure.

Frequency domain correlation-based methods. Poyneer [6] studied the wavefront estimation problem using a SHWFS by observing earth from space using lightweight optics. By assuming periodicity on the input images, the author has pointed out that minimizing the mean squared error (MSE) between both images becomes equivalent to maximizing their periodic convolution, which is efficiently computed in the frequency domain using the cross-correlation theorem. To get subpixel precision the maximum at integer coordinates was refined by independently fitting a parabola on each dimension.

Löfdahl also evaluated a frequency-domain method [21] which, similar to [6], computes the covariance in the Fourier domain (CFF). However, both images were previously normalized to zero mean and windowed with a 2D Hamming window or a flat-top window to avoid ringing caused by the periodization. Again, the subpixel maximum was obtained by fitting a parabola to the grid.

B. Phase Correlation

The phase-correlation method was widely studied in the image-processing domain [25,28]. If we let $I(i, j)$ be an $M \times N$ image, due to the Fourier shift theorem we know that

$$\mathcal{F}\{I(i - \Delta_x, j - \Delta_y)\} = \hat{I}(u, v) \exp\left(-j2\pi\left(\frac{u\Delta_x}{M} + \frac{v\Delta_y}{N}\right)\right).$$

(1)

Then by computing the cross-power spectrum between both images and extracting the phase for each frequency, the matrix ϕ, called the phase correlation matrix, is given by

$$\arg(\hat{C})(u, v) = \phi(u, v) = 2\pi\left(\frac{u\Delta_x}{M} + \frac{v\Delta_y}{N}\right). \qquad (2)$$

The shifts can therefore be computed directly in the frequency domain by fitting a plane passing through the origin of $\phi(u, v)$. Due to aliasing, some of these frequencies may be corrupted and distort the shift estimation. To avoid this problem Knutsson *et al.* [24] discarded most of the corrupted frequencies from ϕ, retaining only two or four of the lowest frequencies. This estimate has the advantage of being the least sensitive to aliasing [25] and hence the most reliable. Moreover, assuming small shifts (smaller than half pixel), no phase unwrapping is required [29]. The accuracy of these methods, however, suffers considerably in low SNR situations [6].

C. Iterated Estimation

Since correlation-based shift estimation has a bias proportional to the shift magnitude [30], then compensating the shift by resampling one of the images and iterating should progressively reduce this bias (see Section 3).

Sidick *et al.* [22] proposed adaptive cross-correlation (ACC) that estimates the shift using an approach similar to Knutsson [24] and used this estimation to resample the second image in the frequency domain to iterate the procedure. Due to potential ringing artifacts on the image boundaries after the resampling procedure, the shift was estimated using the central part of both images with size $N/2$, involving 25% of the image pixels in the computation. To make the shift estimation more accurate, it uses eight frequency components $\phi(n, m)$ with $0 \leq m, n \leq 2$ to perform the least-squares fitting, excluding the center. This procedure is made iterative by accumulating both u and v shift estimates, until a predefined amount of iterations is reached or until $\Delta_s = [\Delta_x^2 + \Delta_y^2]^{1/2}$, the increase of both shift estimates, is lower than a predefined tolerance value. This technique is then applied for every subaperture $I_k(i, j)$.

This algorithm was evaluated on simulated scenes by varying the shift between them [22] and by using a real SHWFS configuration testbed [31] produced in NASA's Jet Propulsion Laboratory [32]. By relaxing the tolerance parameter of their iterative scheme, it achieves errors of the order of 0.05 pixels by using between three and six iterations.

This method presents two problems. Since it discards half of each image to perform the shift estimation, it usually fails when the image contents appear away from the center. Also, as in [24], the shift estimation step of the method suffers severely in low SNR scenarios. Because of this issue, the authors updated the method in [23] by replacing this step with Poyneer's periodic-correlation technique [6]. This method, named adaptive periodic correlation (APC), is more tolerant to noise than ACC.

D. Maximum Likelihood Estimator

Gratadour *et al.* [26] studied the performance of the maximum likelihood estimator (MLE) within an AO context. Assuming that the two images I_0 and I_1 are unknown and contaminated with Gaussian noise their method reduces to minimizing

$$\sum_k (4\sigma^2(k))^{-1}|I_1(k) - [I_0(x - x_1)]_{\text{III}}(k)|^2, \qquad (3)$$

with respect to the shift x_1, where $\sigma^2(k)$ is the noise variance at pixel k and $[]_{\text{III}}$ a sampling operator that performs Fourier resampling, which is done by computing the inverse FFT of Eq. (1). To guarantee that the images can be resampled in the Fourier domain they were pre-filtered using a low-pass filter. This minimization was performed using a conjugate gradient method. Although it is an improvement over the typical cross-correlation, it has a high computational cost, which prohibits its implementation on satellites [6,17].

3. ACCURATE SHIFT ESTIMATION USING OPTICAL FLOW IN THE CONTEXT OF A SHWFS

To estimate the shift between two subapertures, we propose the use of a gradient-based shift estimator (GBSE) based on the optical flow equation. The idea behind this methodology, as proposed originally by Lucas and Kanade [33], is to relate

the difference between two successive frames to the spatial intensity gradient of the first image. Given the two images $I_2(x, y) = I_1(x - v_x, y - v_y)$ where v_x and v_y are the unknown shift coefficients, the first order Taylor approximation yields

$$I_1(x, y) - I_2(x, y) \approx v_x \frac{\partial I_1(x, y)}{\partial x} + v_y \frac{\partial I_1(x, y)}{\partial y}. \qquad (4)$$

To estimate the global optical flow between I_1 and I_2, the Lucas–Kanade algorithm assumes a constant flow for every pixel, which allows the construction of an over-determined system of constraint equations $\mathbf{A}\mathbf{v} = \mathbf{b}$, where $\mathbf{A}$ is composed of spatial intensity derivatives and $\mathbf{b}$ has temporal derivatives. Emulating Simoncelli [34], to increase the accuracy of the method by minimizing noise or aliasing influence, we looked for two kernel functions: an anti-symmetric kernel $\mathbf{d}$ to estimate the image gradients and a symmetric kernel $\mathbf{k}$ to pre-filter the images. Using both kernels, matrix $\mathbf{A}$ and vector $\mathbf{b}$ become

$$\mathbf{A} = \begin{pmatrix} (\mathbf{d}_x * I_1)(p_1) & (\mathbf{d}_y * I_1)(p_1) \\ \vdots & \vdots \\ (\mathbf{d}_x * I_1)(p_n) & (\mathbf{d}_y * I_1)(p_n) \end{pmatrix},$$

$$\mathbf{b} = \begin{pmatrix} (\mathbf{k} * (I_1 - I_2))(p_1) \\ \vdots \\ (\mathbf{k} * (I_1 - I_2))(p_n) \end{pmatrix}, \qquad (5)$$

where p_i with $i = 1 \ldots n$ represents the ith pixel and n the image size. The shift is obtained by Moore–Penrose pseudo-inversion

$$\begin{bmatrix} v_x \\ v_y \end{bmatrix} = \underbrace{\begin{bmatrix} \sum I_x^2 & \sum I_x I_y \\ \sum I_x I_y & \sum I_y^2 \end{bmatrix}^{-1}}_{\mathbf{A}^{\mathsf{T}}\mathbf{A}} \underbrace{\begin{bmatrix} \sum I_t I_x \\ \sum I_t I_y \end{bmatrix}}_{\mathbf{A}^{\mathsf{T}}\mathbf{b}}, \qquad (6)$$

where I_x, I_y stands for $\mathbf{d}_x * I_1$ and $\mathbf{d}_y * I_1$, respectively, and $I_t = \mathbf{k} * (I_1 - I_2)$ is the derivative over time.

It is no coincidence that the results of the method depend on the inversion of this second moment matrix. As we will show later, the determinant of this matrix is crucial to determine the limits on the estimation performance. This matrix will be used to discard ill-posed cases before actually performing the shift estimation. The classic rejection case is when the gradient is mostly oriented in a single direction. This unsolvable situation is known as the aperture problem. Section 4 details its detection using the Cramer–Rao lower bounds.

Centering the Taylor development at zero and taking up to the first order term, the method gets systematically biased and becomes less precise as the shift gets larger (i.e., estimated shifts larger than one pixel would not be correctly estimated). Furthermore, the noise in the input images is completely ignored by the algorithm, which also affects its performance. Both these bias sources have been studied in detail in [30,35] and will be addressed next.

A. Iterative Gradient-based Shift Estimator

Instead of dealing with the bias explicitly, Pham *et al.* [30] have shown that both bias sources depend linearly on the shift magnitude, which justifies the use of an iterative method.

The iterative method is able to significantly reduce the bias, provided an appropriate resampling method is used. Algorithm 1 performs k iterations, computing the shift $v[i]$ by solving Eq. (6) (*findshift*), and iterates by reinterpolating the original image I_2 (*Resample*) using the total accumulated shift w. It is a variant of the Lucas–Kanade algorithm [33] known as the inverse compositional algorithm [36], in which the gradients of the reference image are static throughout the iterations, so $(\mathbf{A}^\mathbf{T}\mathbf{A})^{-1}$ is only computed once.

Algorithm 1: Iterative GBSE Method

```
1: procedure ILK (I₁, I₂)              ▷Receives a pair of images
2:    i ← 0; I₂[0] ← I₂; w ← 0;
3:    while i ≤ k do
4:        v[i] ← findshift(I₁, I₂[i])                    ▷Eq. (6)
5:        w ← w + v[i]                        ▷Accumulate total shift
6:        I₂[i + 1] ← Resample(I₂, −w)           ▷Use the original I₂
7:        i ← i + 1
8:    return w                            ▷Return accumulated shift
```

In the next sections we show that the gradient discretization used by *findshift* and the choice of interpolation method for image resampling are crucial to ensure the precision of the GBSE method.

B. Gradient Computation and Image Prefiltering

Gradient computation for optical flow methods has been thoroughly studied [34,37,38]. Since our shift estimation is focused on accuracy and the image size on SHWFS is typically small (usually smaller than 50×50 pixels), using a large kernel for computing image derivatives implies losing valuable boundary values. This constrains the kernel to be compact yet precise and robust to noise. In fact, the impact on the accuracy and the robustness to noise of the gradient computation is a key factor for the final performance of the GBSE method.

Because the method should be computationally fast, only simple schemes could be used. A straightforward candidate is the centered differences kernel $[1, 0, -1]$; however, since the central pixel is ignored in the computation, its precision could be improved by taking contiguous pixels. For this reason, a backward difference kernel $[1, -1]$ would seem more appropriate. However, the corresponding center of this derivative differs for each component, as seen in the middle image of Fig. 3.

A more precise gradient estimation method, illustrated in the right of Fig. 3, computes the derivatives by performing convolution with $\mathbf{d}_x$ and $\mathbf{d}_y$ given by

$$\mathbf{d}_x = \begin{bmatrix} 1/2 & -1/2 \\ 1/2 & -1/2 \end{bmatrix} \qquad \mathbf{d}_y = \begin{bmatrix} 1/2 & 1/2 \\ -1/2 & -1/2 \end{bmatrix}, \quad (7)$$

and computes the vector $\mathbf{b}$ in Eq. (5) by prefiltering both I_1 and I_2 using the half pixel bilinear shift kernel

$$\mathbf{k} = \begin{bmatrix} 1/4 & 1/4 \\ 1/4 & 1/4 \end{bmatrix}. \quad (8)$$

This gradient estimation procedure is called *hypomode* [39], which, despite being simplistic, usually improves the accuracy obtained by GBSE methods using finite difference gradient estimation. This is because it slightly blurs the input images, which alleviates both aliasing and noise.
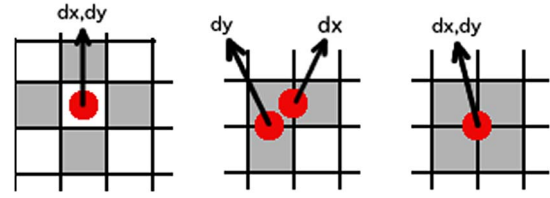

Fig. 3. Used pixels (gray background) for fast gradient estimation methods and their exact localization (red dots). **Left**: Centered differences. **Center**: 1D backward difference for both ∂x and ∂y. **Right**: 2D backward difference.

We also considered the normalized 2D Gaussian smoothing kernel $\mathbf{k} = g(x, y, \sigma_g)$ with standard deviation σ_g, and its derivatives $\mathbf{d}_x = -\frac{x}{\sigma_g^2}g(x, y, \sigma_g)$ and $\mathbf{d}_y = -\frac{y}{\sigma_g^2}g(x, y, \sigma_g)$. The parameter σ_g controls the amount of blur, thus using a small value would be less tolerant to noise, while a high value could remove textures useful for the shift estimation. In our experiments, we evaluated using $\sigma_g = \{0.3, 0.6, 1\}$ with supports of 3, 5 and 7 pixels, respectively.

As seen from both Figs. 4(a) and 4(b), the fastest, most accurate gradient estimator for small shifts (≈ 0.1) is the *hypomode*. Therefore it should be considered when the underlying deformations are small enough, which could happen on a closed loop system with frequent mirror corrections. However, if the maximum shift caused by the wavefront aberration is larger than half a pixel, computing the Gaussian derivatives with $\sigma_g = 0.6$ offers the best balance between accuracy and tolerance against noise, as seen from Figs. 4(c)–4(f). In fact, using $\sigma = 0.6$ gives better results than using $\sigma = 0.3$ because a higher σ removes more noise from the derivatives, and blurring the images affects the accuracy less than neglecting

(a) Max. shift: 0.1 pixels.   **(b)** Max. shift: 0.1 pixels.

(c) Max. shift: 0.5 pixels.   **(d)** Max. shift: 0.5 pixels.

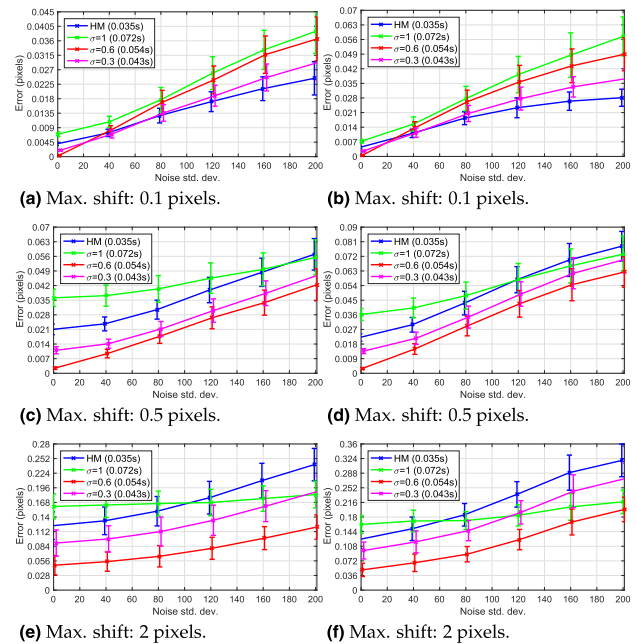**(e)** Max. shift: 2 pixels.   **(f)** Max. shift: 2 pixels.

Fig. 4. Gradient estimation methods comparison for three different maximum shifts (0.1, 0.5, and 2 pixels). **Left**: Highly contrasted image (simple case). **Right**: Gradients mainly distributed on a single direction (challenging case). Noise standard deviation according to 12-bit images.

the noise. Finally, it should be noted that although taking $\sigma = 1$ usually offers poor accuracy with small image sizes, its tolerance to noise becomes a decisive factor as the noise increases, as seen in Figs. 4(e) and 4(f).

C. Interpolation Methods for Image Resampling

To iterate the method, the second image must be shifted, as indicated in step 6 of Algorithm 1. To this end, we evaluated five different interpolation methods : bilinear, bicubic [40], and cubic spline [41], together with resampling using the Fourier shift theorem [42], which we evaluated with and without image periodization. Image periodization prevents the generation of ringing artifacts due to the discontinuities at the image boundaries. It amounts to using a discrete Fourier transform (DFT) to resample a mirrored version of the image that has no discontinuities when periodization is assumed (Fig. 5).

The overall accuracy of the method depends on the choice of interpolation method. However, precision comes at a higher processing cost. We evaluated the different interpolations by simulating a landscape with noise of $\sigma_n = 80$, displacements between subapertures of up to 2 pixels, and computing gradients by using Gaussian derivatives with $\sigma_g = 0.6$. For each method, we computed the average error and standard deviation over 200 independent random realizations, using the GBSE method with two and three iterations. Figure 6 shows a non-negligible performance difference between the methods. In terms of average error, both DFT-based methods achieve the best results; however, we obtained no significant improvement by performing periodization, although we observed a minimal reduction in the standard deviation. Although the splines interpolation yields slightly less accurate results, it should be considered if fast DFT hardware cannot be installed. Finally, both bicubic and bilinear interpolation perform significantly worse than the rest, although bicubic interpolation results had less variability with respect to other approaches. Finally, using three iterations does not improve the results considerably compared to using two, so there is no justification for an increase in the computational cost. However, although we have not shown this outcome in this experiment, this difference gets higher as the noise increases, which would justify its use.

D. Image Intensities Equalization

One requirement of the GBSE algorithm is to work on images with similar intensities. Since occluded subapertures receive less light, their intensities differ from the reference image. To this end, we equalized all subimages by normalizing their mean with the highest mean among all subapertures. When the
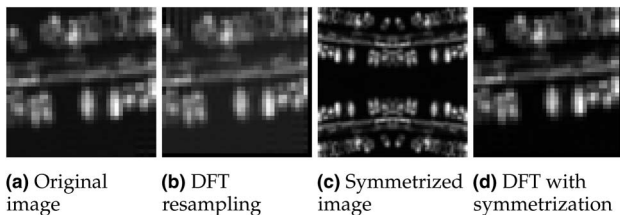

(a) Original image   **(b)** DFT resampling   **(c)** Symmetrized image   **(d)** DFT with symmetrization

Fig. 5. Example of FFT resampling with and without image symmetrization. Resampling with DFT produces ringing due to the discontinuities at the periodized boundaries. We observed no visible ringing after resampling with symmetrization.
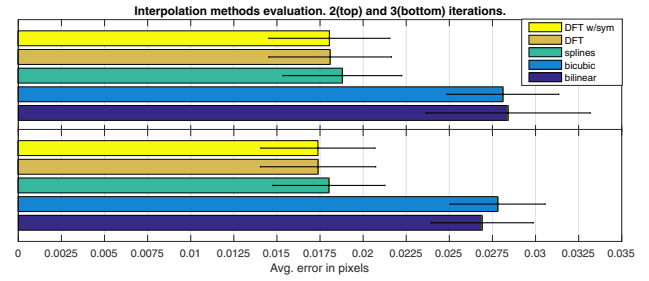

Fig. 6. Comparison of evaluated interpolation methods using two and three iterations and Gaussian derivatives with $\sigma_g = 0.6$. We fixed image noise at $\sigma_n = 80$ and set the maximum displacement to 2 pixels.

point-spread function (PSF) of each subaperture is known, another equalization strategy before shift estimation between a subaperture and the reference is to convolve both images with the PSF of the other one [8]. Because our focus was on the shift estimation method, we chose to perform the equalization by the simple procedure explained earlier. It is computationally cheaper, yet offers excellent results.

E. Multiscale Implementation

The GBSE algorithm can be easily adapted to work in an open loop environment where aberrations are potentially larger, leading to larger shifts between subapertures. As mentioned before, if the shift is larger than one pixel, the GBSE method fails. However, by building a pyramid representation of the input images, Eq. (6) can be applied on each scale to estimate the shift between images, and this estimated shift can then be used to resample the second image on the following level of the pyramid. If more accuracy is desired, Algorithm 1 can be used to better estimate the shift at each scale. We computed the pyramid using an approximate dyadic Gaussian pyramid [43]. Starting from the coarse image at scale $n > 1$, Algorithm 2 summarizes this method.

Algorithm 2: Multiscale GBSE Method

1: **procedure** MSSE (I_1, I_2) ▷Receives a pair of images
2:   $I_1^{1\dots n} \leftarrow BuildPyramid(I_1, n)$ ▷Burt and Adelson's Gaussian Pyramid [43]
3:   $I_2^{1\dots n} \leftarrow BuildPyramid(I_2, n)$ ▷i.e., impyramid function from Matlab
4:   $i \leftarrow n; w \leftarrow 0$ ▷n: number of scales, w: accumulated shift
5:   **while** $i > 1$ **do**
6:    $v(i) \leftarrow ILK(I_1^i, I_2^i)$ or $findshift(I_1^i, I_2^i)$ ▷Alg. 1 or Eq. (6)
7:    $w \leftarrow 2w + 2v(i)$
8:    $I_2^{i-1} \leftarrow Resample(I_2^{i-1}, -w)$
9:    $i \leftarrow i - 1$
10:   $v(1) = findshift(I_1^1, I_2^1)$
11:   **return** $w + v(1)$ ▷Return accumulated shift

4. SCENE PRESELECTION AND ROBUSTNESS ESTIMATION

Before evaluating the deformation of the incoming wavefront, it is crucial to determine if the current landscape (i.e., what the satellite is observing at that moment), is suitable to perform wavefront sensing. Sidick *et al.* [31] and Poyneer [6] studied

this problem and proposed several fail-safe criteria to determine if the current landscape is acceptable.

In this context, we performed two distinct validations to ensure an accurate wavefront correction. While the first one was based on calculating the lowest theoretical achievable error through the Cramer–Rao lower bound (CRLB) given by the noise and the image contents, the second validation, called the eigenratio test, measured the gradient distribution along the image through the ratio of the eigenvalues of the structure tensor. Both validations are complementary and should be verified together.

CRLB test. The Cramer–Rao lower bound allows to predict the best achievable accuracy, given the current landscape and the underlying noise. In the last decade, three main works have addressed the calculation of the error on the estimated shift caused by noise. Robinson and Milanfar [35] used the Cramer–Rao lower bound to derive a performance limit for image registration. The CRLB imposes a lower limit on the MSE for any estimate of a deterministic parameter. Pham *et al.* [30] continued on the same idea to derive a theoretical limit for image registration, followed by a study of the bias for the gradient-based 2D shift estimation. Recently, Aguerrebere *et al.* [44] performed an in-depth study of performance limits within a multi-image alignment context and derived several Cramer–Rao lower bounds, depending on the conditioning of the problem.

By assuming that the noise is independent, homoscedastic, Gaussian, and with the same variance σ_n^2 on both images, and denoting by S the set of all pixels in the image, the Cramer–Rao bound for any unbiased 2D shift estimator is

$$\text{var}(v_x) \geq \frac{\sigma_n^2 \sum_S I_y^2}{\text{Det}} \qquad \text{var}(v_y) \geq \frac{\sigma_n^2 \sum_S I_x^2}{\text{Det}}, \qquad (9)$$

where $\text{Det} = \sum_S I_x^2 \sum_S I_y^2 - (\sum_S I_x I_y)^2$. We can therefore define a parameter Δ_{CRLB}, the maximum allowed error in pixels, that determines whether the current landscape is acceptable to perform wavefront estimation, by verifying

$$(\text{var}(v_x) + \text{var}(v_y))^{1/2} \leq \Delta_{\text{CRLB}}. \qquad (10)$$

Yet, I_x, I_y represent the gradient obtained from the unknown noiseless image I. Thus, this bound is only useful for a theoretical study. In practice, however, the required values can be approximated using the method in [45], where Pham and Duggan estimated the second moment matrix of image I_1 from noisy versions $\tilde{I}_1$ and $\tilde{I}_2$. Another possibility would be to approximate these sums by computing the expected value using the derivative definition and a noise variance estimation. For example, set $I_x(i,j) = I(i+1, j) - I(i,j)$ and let $\tilde{I} = I + n$ be the observed noisy image where n has distribution $\mathcal{N}(0, \sigma_n^2)$. Since all $n(i,j)$ are independent, by the law of large numbers we have

$$\sum_S \tilde{I}_x^2 = \sum_S (I_x + n_x)^2$$

$$= \sum_S I_x^2 + \sum_S I_x n_x + \sum_S n_x^2 \simeq \sum_S I_x^2 + 2|S|\sigma_n^2.$$

It follows that we can estimate $\sum_S I_x^2$ from the noisy image $\tilde{I}$ by

$$\sum_S I_x^2 \simeq \sum_S \tilde{I}_x^2 - 2|S|\sigma_n^2. \qquad (11)$$

The other terms can be computed using similar calculations.

The CRLB defined in Eq. (9) expresses a direct relationship between the accuracy of the estimation and the SNR ratio, measured as a ratio of the noise to the square of the gradient. Furthermore, it follows from the form of the denominator of these expressions that if there is a strong correlation between I_x and I_y, the vertical and horizontal partial derivatives, then Det will be zero or very close to zero. The formulas show that this entails a high variance for the estimation of the translation. This is the so-called aperture problem [46]. In that case the true motion is irrecoverable.

It must be noted that the Cramer–Rao bounds were derived for an unbiased 2D shift estimation. For the case of biased estimators, the bound is even higher. Also, the hypothesis made about the noise being white Gaussian and homoscedastic does not hold in a SHWFS context used from earth observation satellites. However, the sensor's noise model is usually known beforehand, which allows its variance to be stabilized by applying a variance stabilization transform (VST) such as the well-known Anscombe transform [47].

Finally, for SHWFS, since shifts between images are independent, we can impose the limit on the registration accuracy by estimating the shift between two frames.

Eigenratio test. As noted by [44], the CRLB is less precise where it is most needed, namely when the signal is dominated by noise. Indeed, in that case the numerator and denominator of Eq. (9) cannot be estimated reliably, being both the difference of equivalent terms. Therefore, we must use more robust safety computations.

We have proposed to rapidly discard a landscape for a shift estimation by involving the eigenratio score of the second moment matrix $\tau = \mathbf{A^T A}$ of Eq. (6). The matrix τ is also the structure tensor with unit weights associated to the image I_1. The eigenvalues λ_1, λ_2 of τ and their corresponding eigenvectors e_1, e_2 summarize the distribution of the image gradient $\nabla I = (I_x, I_y)$. Namely, if $\lambda_1 > \lambda_2$, then e_1 (or $-e_1$) is the direction that is maximally aligned with the gradient within the image. More generally, the value of λ_k, for $k \in \{1, 2\}$, is the average of the square of the directional derivative of I along e_k. The relative discrepancy between the two eigenvalues is an indicator of the degree of anisotropy of the gradient in the image, measuring how strongly it is biased toward a particular direction (and its opposite). Then by calculating the ratio λ_2/λ_1, we obtain a number between 0 and 1, characterizing the dominance of a particular direction for the gradients of the image. We empirically verified that a ratio $\lambda_2/\lambda_1 < 0.2$ effectively degrades the shift estimation task, and this metric could be used to discard badly conditioned situations.

To compute this ratio, since $\tau = \mathbf{A}^T\mathbf{A}$ is positive definite and symmetric, then both of its eigenvalues λ_1 and λ_2 are real and non-negative and its computation is straightforward.

5. RESULTS

A. Scene Pre-selection Evaluation

Figures 7(a) and 7(b) display two examples of SH landscapes that do not validate the eigenratio test. In these images, there is a strong dominant gradient direction that complicates the shift estimation. The aperture problem is visually obvious in both cases. Figures 7(c) and 7(d) present a high CRLB. The first
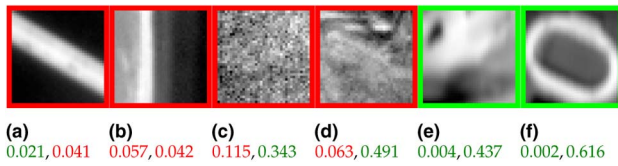
Fig. 7. CRLB and eigenratios, respectively, for six examples of land-scapes. Green represents valid and red implies failure.

one corresponds to a project where the images are composed only by noise. The second example has a higher SNR, but the noise is still considerable. Figures 7(e) and 7(f) show two examples of valid landscapes that were validated by both proposed tests.

B. Comparison with State-of-the-art Methods

1. CNES Simulated Database

CNES, the French space agency, provided realistic simulations of several SHWFS landscapes obtained from earth-observing satellites with their corresponding ground truth. The provided images were 37 × 37 pixels from a 12 × 12 grid following the occlusion schema of Fig. 2(a). The simulated wavefront aberrations translated into displacements no larger than half a pixel. For each provided landscape, three different SNR settings were simulated. Figure 8 displays some example landscapes.

We tested every described state-of-the-art algorithm and our proposed method using different interpolation/gradient estimation approaches against the whole dataset. Table 1 displays the errors in pixels for the best performing methods. These are the method from Michau et al. [20], the SDF method performing 2D quadratic interpolation (SDF-2QI) from Lofdahl [21], the periodic convolution approach from Poyneer [6], and the iterative APC method from Sidick et al. [23]. For the proposed GBSE approach, we considered three variants, with increasing computational cost. We also included a fourth variant using the Gaussian derivative estimation method for comparison.

The errors obtained for Figs. 8(a) and 8(b) are close to the theoretical limits predicted by their CRLB. On the other side, the error obtained with Fig. 8(c) and its CRLB implies that a strong improvement is possible. Line 4, corresponding to Fig. 8(d), is an example where every method fails to achieve accurate results, possibly due to the noise and the lack of texture, which is revealed by a lower bound considerably higher than for most other cases. Figure 8(e) shows an example of a landscape where the Poyneer method [6] as well as PCC [23] are clearly improved by the proposed approach. Figure 8(f) proves that the aperture problem hinders most shift estimation methods, as evidenced by their resulting errors. The PCC
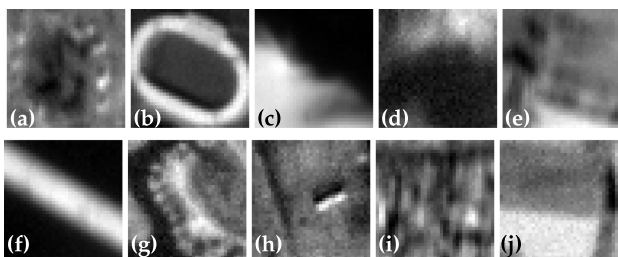
algorithm particularly failed under the landscape present in Fig. 8(g), although the reason is not evident. Finally, line 9 [Fig. 8(i)] shows a case where the SDF-2QI method was outperformed by all variants of the proposed approach.

2. Simulated Experiments

Experimental setup. We used a simulator to evaluate the performance of the proposed method. Given a 12-bit input image, we generated a set of images matching a SHWFS configuration provided by CNES. We assumed a 12 × 12 lenslet grid, occluded as shown in Fig. 2(a). For each lenslet we randomly generated a ground truth shift. Since we were simulating in a closed loop environment, we kept the maximum displacement to half a pixel. We then obtained each subaperture image by DFT resampling the input image, extracting a 37 × 37 pixels subimage, multiplying by the occlusion factor, and finally adding noise.

We computed the error for each method as the mean error for all valid subapertures. A subaperture was considered invalid and therefore discarded if it was occluded on more than 60% of its surface. The error for each subaperture was the Euclidean distance between the measured and the ground truth shift. To evaluate the robustness to image content, we used three subimages: a highly contrasted one that should not present any difficulty for shift estimation, a slightly more challenging one with its gradient mainly distributed on a single direction, and one from the sea with almost no signal (there are just a few pixels of land on the bottom). Different amounts of additive white Gaussian noise were simulated (with standard deviation $\sigma_n \in [1, \ldots, 150]$), and we evaluated all methods on 100 noise realizations. Figure 9 shows the subimages affected by three noise levels. We handled signal dependent noise by applying a variance stabilization transform. Finally, we measured the processing time of each method using a non-optimized Matlab implementation on an Intel Xeon E5-2650 CPU.

We tested several variants of the proposed GBSE method. Each one was composed by an interpolation method for resampling selected among the five methods proposed (Section 3.C), a gradient estimation method chosen between the *hypomode* or one of the three Gaussian derivatives with $\sigma_g = \{0.3, 0.6, 1\}$ (Section 3.B), and using up to three iterations per shift estimation. Also, we evaluated different variants using the multiscale approach (Section 3.E) up to three scales, where for each scale, we used an iterative GBSE algorithm with up to three iterations. From these methods we retained the best performing non-iterative method ($k = 1$ and no resampling), which uses $\sigma_g = 0.6$ for the gradient computation, and the best one with three iterations, which uses DFT resampling with image periodization and $\sigma_g = 0.3$. We compared them with all state-of-the-art algorithms presented in Section 2. For practical reasons, we have only displayed the best performing ones, namely, the ACC [22] and the APC [23] methods from Sidick presented in Section 3.C, and the Poyneer [6] and Löfdahl SDF-2QI algorithm [21] presented in Section 3.A. The SDF-2QI algorithm computes the squared sum difference function and searches its maximum by using 2D quadratic interpolation. We also evaluated all other presented methods, but we discarded them due to lower accuracies.

Fig. 8. Examples of landscapes from the CNES database.

Table 1.   CRLB, Eigenratio (ER) and Errors (in Pixels) for Selected Sample Landscapes from the CNES Database[a]

	CRLB	ER	[21]	[20]	[6]	[23]	1it	2it L	3it S	1it $\sigma = 0.6$
(1)	**0.014**	**0.66**	**0.019**	**0.121**	**0.026**	**0.054**	**0.030**	**0.017**	<u>**0.016**</u>	**0.022**
(2)	**0.006**	**0.44**	**0.029**	**0.106**	**0.038**	**0.158**	**0.014**	**0.008**	<u>**0.008**</u>	**0.013**
(3)	*0.006*	*0.19*	*0.048*	*0.096*	*0.105*	*0.092*	<u>*0.035*</u>	*0.036*	*0.036*	*0.040*
(4)	*0.041*	**0.59**	*0.127*	*0.113*	*0.090*	*0.794*	*0.070*	<u>*0.064*</u>	*0.069*	*0.078*
(5)	**0.011**	**0.77**	**0.039**	**0.113**	**0.069**	**0.070**	**0.026**	**0.016**	<u>**0.016**</u>	**0.022**
(6)	*0.030*	*0.01*	*0.081*	*0.099*	*0.083*	*0.081*	*0.053*	*0.043*	<u>*0.040*</u>	*0.042*
(7)	**0.019**	**0.69**	**0.023**	**0.111**	**0.048**	**0.134**	**0.034**	**0.021**	<u>**0.021**</u>	**0.025**
(8)	*0.026*	*0.63*	*0.045*	*0.114*	*0.039*	*0.083*	*0.048*	*0.032*	<u>*0.031*</u>	*0.037*
(9)	**0.010**	**0.34**	**0.043**	**0.113**	**0.029**	**0.042**	**0.028**	**0.015**	<u>**0.014**</u>	**0.021**
(10)	*0.027*	**0.61**	*0.065*	*0.112*	*0.051*	*0.645*	*0.046*	<u>*0.037*</u>	*0.043*	*0.047*
Avg.	0.029	132	0.146	0.111	0.491	0.478	0.047	<u>0.039</u>	0.039	0.043
Valid	0.011	64	0.024	0.110	0.048	0.057	0.027	0.018	<u>0.017</u>	0.022
Time			0.296	0.025	0.084	0.221	0.034	0.165	0.311	0.052

[a]Rows in bold represent landscapes considered valid (CRLB < 0.02 and ER > 0.2), while invalid landscapes are shown in italic. Underline indicates lowest error. Averages correspond to the whole dataset, and its ER column displays the amount of landscapes processed. The Valid row represents the averages over all valid landscapes. The first column links each row with the landscapes shown in Fig. 8. Columns [21,20,6] and [23] refer to SDF-2QI, Michau *et al.*, Poyneer and APC methods, respectively. The variants of our approach 1it, 2it L, 3it S represent Algorithm 1 using the *hypomode* derivative with one, two (bilinear interpolation), and three (spline interpolation) iterations, respectively. The last column stands for one iteration and Gaussian derivative with $\sigma = 0.6$.

Results in a closed loop system. We compared iterative and non-iterative algorithms separately. The average errors and the standard deviations for non-iterating methods on the first image type are shown in Fig. 10 (top left), together with the processing time. The non-iterative GBSE version using Gaussian derivatives with $\sigma = 0.6$ outperforms both Poyneer and SDF-2QI (which perform similarly in this image). GBSE is also more stable (less variability) and faster. Figure 10 (top right) compares both iterative methods ACC and APC with GBSE using three iterations, DFT resampling, and the *hypomode* derivative. Again, the proposed method proved to be the most accurate and more stable. Even more, this method is the best compared to non-iterated methods as well. Notice the high impact of noise on the ACC method. It is more precise than both non-iterating methods for low noise ($\sigma \leq 20$). Nevertheless, it diverges for stronger noise. This problem is a well-known issue for phase-correlation methods [6].

The results for the second image type (bottom of Fig. 10) are similar to the first one, although the average errors are higher. While the SDF-2QI performs slightly worse, the Poyneer method is considerably worse because of discrepancies at the image boundaries resulting from the periodicity assumption of the periodic convolution used by Poyneer. This result also explains why both ACC and PCC methods behave so poorly on this image. It also implies that computing the shift in the spatial domain is usually more stable than doing so in the frequency domain, unless some windowing is performed, which is prohibitive on such small images where the objects are sometimes close to the image boundaries. Yet again, the proposed methods are more precise and stable, with less variability than the state-of-the-art options. The third image type did not pass the verification step and all the methods failed, so its results have been omitted.

Results under larger displacements. We performed the same experiment by simulating wavefront aberrations with displacements of up to four pixels to evaluate robustness against high frequency aberrations. Figure 11 shows the average error together with the standard deviations for the most representative methods. Due to the larger underlying displacements, multiscale approaches achieve better results as the noise increases, reproducing the results of [48]. In fact, a multiscale approach becomes mandatory if fewer than two iterations are performed, and the best performing method used three scales (where a single iteration was used in the coarsest scale, two iterations with FFTP interpolation in the second scale and three iterations with FFTP interpolation in the final finer
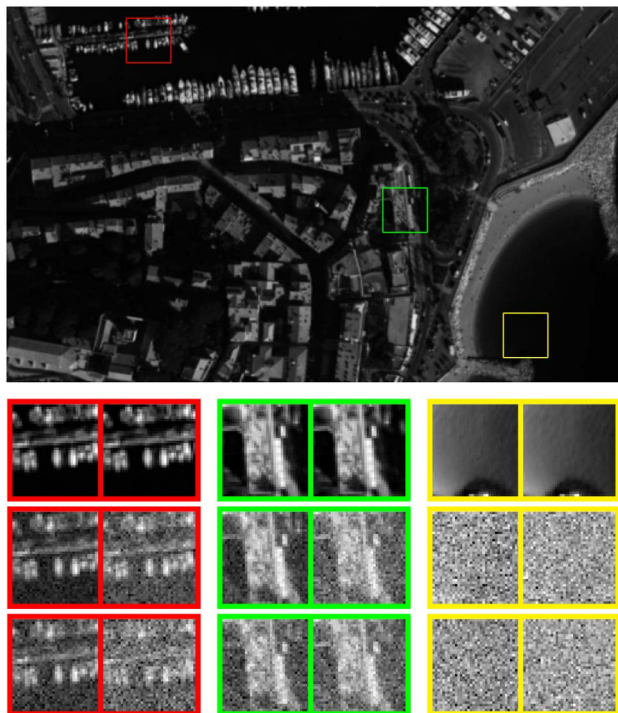

Fig. 9.   Top: Input image used for the simulations. **Bottom**: For each level of noise $\sigma_n = \{1, 100, 200\}$ (vertically separated), two different subapertures are shown: no occlusion and 57% occluded (horizontally separated). The dynamic ranges were stretched for viewing purposes.
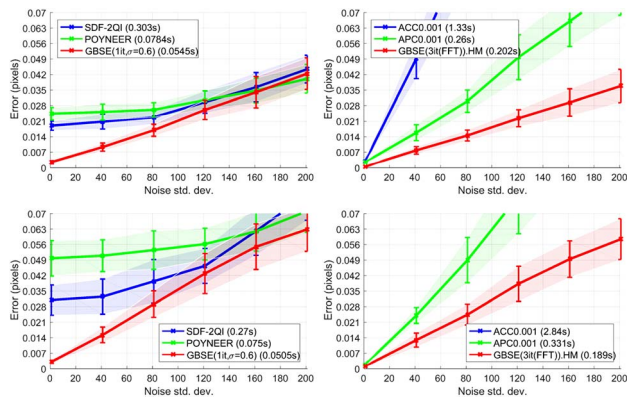
Fig. 10. Performance for non-iterative and iterative methods compared to the best variant of the proposed GBSE approach. **Top**: First test image. **Bottom**: Second test image. **Left**: Non-iterative methods. **Right**: Iterative methods.
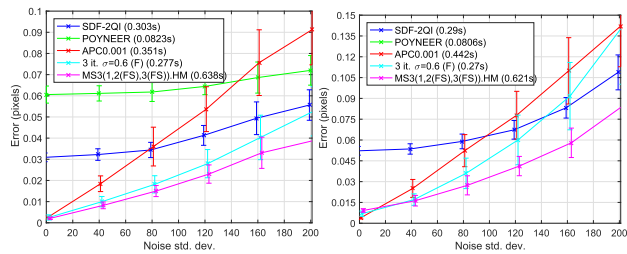

Fig. 11. Average error and standard deviations of selected methods and two variants of the proposed GBSE approach when simulating wavefront aberrations yielding displacements of up to 4 pixels. **Left**: First test image. **Right**: Second test image.

scale). Although this method was the most accurate in our tests, it also required more computational resources as evidenced by its running time. However, using the iterative non-multiscale approach with three iterations and FFT interpolation showed comparable results but required less processing time. Nevertheless, the method proposed by Poyneer should be considered when lower processing times are required. As expected, non-iterated versions of the GBSE algorithm failed when estimating the shift with large underlying displacements. Let us add a caveat that when measuring the aberration using the second, slightly challenging, landscape (green rectangle in Fig. 9), the Poyneer method obtained inaccurate results even under high SNR conditions.

6. CONCLUSION

We have proposed a new method to accurately estimate sub-pixel shift, based on an iterative global optical flow method, in the context of a SHWFS on extended scenes for onboard aberration correction on earth observation satellites. Using a telescope simulator developed by CNES, we have shown that the proposed algorithm is more accurate, stable, robust to noise, and has lower variability than the current state-of-the-art, permitting a more precise wavefront estimation. By performing onboard, real-time mirror correction, this research

opens the door to cheaper, high-resolution earth observation satellites.

Although this method was conceived for onboard earth observation satellites, it could also be used in a ground-based wavefront-sensing context. Indeed, for ground-based applications, the processing time requirements existing in satellites are considerably lower. Due to the availability of more computational resources, the proposed method could still be applicable using more iterations and/or scales. Therefore, we have envisaged testing the proposed algorithm to correct the undesired effects of atmospheric turbulence on extended sources.

REFERENCES

1. P. Wizinowich, D. S. Acton, C. Shelton, P. Stomski, J. Gathright, K. Ho, W. Lupton, K. Tsubota, O. Lai, C. Max, J. Brase, J. An, K. Avicola, S. Olivier, D. Gavel, B. Macintosh, A. Ghez, and J. Larkin, "First light adaptive optics images from the Keck II telescope: a new era of high angular resolution imagery," Publ. Astron. Soc. Pac. **112**, 315–319 (2000).
2. A. Wirth, "Ophthalmic instrument having Hartmann wavefront sensor with extended source," U.S. patent 6,595,642 (22 July 2003).
3. M. J. Booth, "Adaptive optics in microscopy," Philos. Trans. R. Soc. London A **365**, 2829–2843 (2007).
4. R. K. Tyson, "Bit-error rate for free-space adaptive optics laser communications," J. Opt. Soc. Am. A **19**, 753–758 (2002).
5. R. Tyson, *Principles of Adaptive Optics* (CRC, 2010).
6. L. A. Poyneer, "Scene-based Shack–Hartmann wave-front sensing: analysis and simulation," Appl. Opt. **42**, 5807–5815 (2003).
7. C. Escolle, E. Hugot, T. Fusco, M. Ferrari, V. Michau, and T. Bret-Dibat, "Adapting large lightweight primary mirror to space active optics capabilities," Proc. SPIE **9151**, 915128 (2014).
8. A. M. Bonnefois, T. Fusco, S. Meimon, V. Michau, L. Mugnier, J. F. Sauvage, C. Engel, C. Escolle, M. Ferrari, E. Hugot, A. Liotard, M. Bernot, M. Carlavan, F. Falzon, T. Bret-Dibat, and D. Laubier, "Comparative theoretical and experimental study of a Shack–Hartmann and a phase diversity sensor, for high-precision wavefront sensing dedicated to space active optics," in *ICSO* (2014).
9. P. C. Chen, C. W. Bowers, M. Marzouk, and R. C. Romeo, "Advances in very lightweight composite mirror technology," Opt. Eng. **39**, 2320–2329 (2000).
10. L. A. Poyneer, D. W. Palmer, K. N. LaFortune, and B. Bauman, "Experimental results for correlation-based wavefront sensing," in *Optics and Photonics*, M. T. Gruneisen, J. D. Gonglewski, and M. K. Giles, eds. (International Society for Optics and Photonics, 2005), pp. 58940N.
11. C. Robert, J.-M. Conan, V. Michau, T. Fusco, and N. Vedrenne, "Scintillation and phase anisoplanatism in Shack–Hartmann wave-front sensing," J. Opt. Soc. Am. A **23**, 613–624 (2006).
12. N. Védrenne, V. Michau, C. Robert, and J.-M. Conan, "Shack–Hartmann wavefront estimation with extended sources: anisoplanatism influence," J. Opt. Soc. Am. A **24**, 2980–2993 (2007).
13. W. H. Southwell, "Wave-front estimation from wave-front slope measurements," J. Opt. Soc. Am. A **70**, 998–1006 (1980).
14. J. Herrmann, "Least-squares wave front errors of minimum norm," J. Opt. Soc. Am. A **70**, 28–35 (1980).
15. L. A. Poyneer, D. T. Gavel, and J. M. Brase, "Fast wave-front reconstruction in large adaptive optics systems with use of the Fourier transform," J. Opt. Soc. Am. A **19**, 2100–2111 (2002).

16. M. Roopashree, A. Vyas, and B. R. Prasad, "Performance analysis of Fourier and vector matrix multiply methods for phase reconstruction from slope measurements," arXiv e-prints (2009).

17. V. Michau, J.-M. Conan, T. Fusco, M. Nicolle, C. Robert, M.-T. Velluet, and E. Piganeau, "Shack–Hartmann wavefront sensing with extended sources," Proc. SPIE **6303**, 63030B (2006).

18. G. Rousset, "Wave-front sensors," Adapt. Opt. Astron. **1**, 91–130 (1999).

19. B. C. Platt and R. Shack, "History and principles of Shack–Hartmann wavefront sensing," J. Refractive Surg. **17**, S573–S577 (2001).

20. V. Michau, G. Rousset, and J. Fontanella, "Wavefront sensing from extended sources," in *Real Time and Post Facto Solar Image Correction*, Sunspot, New Mexico, 1993, vol. **1**, p. 124.

21. M. G. Löfdahl, "Evaluation of image-shift measurement algorithms for solar Shack–Hartmann wavefront sensors," Astron. Astrophys. **524**, A90 (2010).

22. E. Sidick, J. J. Green, C. M. Ohara, and D. C. Redding, "An adaptive cross-correlation algorithm for extended scene Shack–Hartmann wavefront sensing," in *Adaptive Optics: Methods, Analysis and Applications* (Optical Society of America, 2007).

23. E. Sidick, "Adaptive periodic-correlation algorithm for extended scene Shack–Hartmann wavefront sensing," in *Imaging and Applied Optics* (Optical Society of America, 2011), paper CPDP1.

24. P. Knutsson, M. Owner-Petersen, and C. Dainty, "Extended object wavefront sensing based on the correlation spectrum phase," Opt. Express **13**, 9527–9536 (2005).

25. H. Stone, M. Orchard, E.-C. Chang, and S. Martucci, "A fast direct Fourier-based algorithm for subpixel registration of images," IEEE Trans. Geosci. Remote Sens. **39**, 2235–2243 (2001).

26. D. Gratadour, L. Mugnier, and D. Rouan, "Subpixel image registration with a maximum likelihood estimator," Astron. Astrophys. **443**, 357–365 (2005).

27. T. Tarbell and R. Smithson, "A simple image motion compensation system for solar observations," *Solar Instrumentation: What's Next? Proceedings of a Conference* (1981).

28. H. Foroosh, J. Zerubia, and M. Berthod, "Extension of phase correlation to subpixel registration," IEEE Trans. Image Process. **11**, 188–200 (2002).

29. D. C. Ghiglia and M. D. Pritt, *Two-dimensional Phase Unwrapping: Theory, Algorithms, and Software* (Wiley, 1998), Vol. **4**.

30. T. Q. Pham, M. Bezuijen, L. J. Van Vliet, K. Schutte, and C. L. L. Hendriks, "Performance of optimal registration estimators," Proc. SPIE **5817**, 133–144 (2005).

31. E. Sidick, R. Morgan, J. Green, C. Ohara, and D. Redding, "Adaptive cross-correlation algorithm and experiment of extended scene Shack–Hartmann wavefront sensing," Proc. SPIE **6687**, 668710 (2007).

32. R. M. Morgan, K. V. Shcheglov, J. J. Green, C. M. Ohara, J. Roberts, and E. Sidick, "Testbed for extended-scene Shack–Hartmann and phase retrieval wavefront sensing," in *Optics and Photonics* (International Society for Optics and Photonics, 2005), pp. 59030I.

33. B. D. Lucas and T. Kanade, "An iterative image registration technique with an application to stereo vision," in *IJCAI* (Morgan Kaufmann, 1981), pp. 674–679.

34. E. Simoncelli, "Design of multi-dimensional derivative filters," in *IEEE International Conference on Image Processing (ICIP)*, Austin, 1994, Vol. **1**, pp. 790–794.

35. D. Robinson and P. Milanfar, "Fundamental performance limits in image registration," IEEE Trans. Image Process. **13**, 1185–1199 (2004).

36. S. Baker and I. Matthews, "Lucas–Kanade 20 years on: a unifying framework," Int. J. Comput. Vis. **56**, 221–255 (2004).

37. M. Elad, P. Teo, and Y. Hel-Or, "Optimal filters for gradient-based motion estimation," in *Proceedings of the Seventh IEEE International Conference on Computer Vision* (IEEE, 1999), vol. **1**, pp. 559–565.

38. D. Robinson and P. Milanfar, "Bias minimizing filter design for gradient-based image registration," Signal Process. **20**, 554–568 (2005). Special Issue on Advanced Aspects of Motion Estimation.

39. B. Rouge, H. Vadon, and A. Giros, "Fine stereoscopic image matching and dedicated instrument having a low stereoscopic coefficient," U.S. patent 8,064,687 (22 November 2011).

40. R. Keys, "Cubic convolution interpolation for digital image processing," IEEE Trans. Acoust. Speech Signal Process. **29**, 1153–1160 (1981).

41. C. De Boor, *A Practical Guide to Splines (Applied Mathematical Sciences)*, rev. ed. (Springer, 2001).

42. G. M. Bernstein and D. Gruen, "Resampling images in Fourier domain," Publ. Astron. Soc. Pac. **126**, 287–295 (2014).

43. P. J. Burt and E. H. Adelson, "The Laplacian pyramid as a compact image code," IEEE Trans. Commun. **31**, 532–540 (1983).

44. C. Aguerrebere, M. Delbracio, A. Bartesaghi, and G. Sapiro, "Fundamental limits in multi-image alignment," arXiv: 1602.01541 (2016).

45. T. Pham and M. Duggan, "Bidirectinal bias correction for gradient-based shift estimation," in *15th IEEE International Conference on Image Processing (ICIP)* (IEEE, 2008), pp. 829–832.

46. S. Shimojo, G. H. Silverman, and K. Nakayama, "Occlusion and the solution to the aperture problem for motion," Vis. Res. **29**, 619–626 (1989).

47. F. J. Anscombe, "The transformation of Poisson, binomial and negative-binomial data," Biometrika **35**, 246–254 (1948).

48. M. Rais, J.-M. Morel, and G. Facciolo, "Iterative gradient-based shift estimation: to multiscale or not to multiscale?" in *Progress in Pattern Recognition, Image Analysis, Computer Vision, and Applications*, Montevideo, Uruguay, 2015, pp. 416–423.